# Chapter 5
# The Phantom Force

**Alfred John Weymouth and Franz J. Giessibl**

**Abstract** While atomic resolution in an AFM image is usually assumed to originate from the formation of a chemical bond or Pauli repulsion, it can also be caused by a phenomenon we called the phantom force. When there is an electric potential difference between tip and sample, they will be attracted to one another. It is quite common in AFM experiments to apply a voltage between the tip and the sample. At distances required for atomic resolution, this can result in a tunneling current. If there is a tunneling current, then there will also be a potential difference within the sample (as charge carriers do not accumulate after they have tunnelled). The magnitude of this potential difference within the sample is related to the resistivity of the sample. The total potential difference between the sample bulk and the tip is fixed by the applied voltage, so any potential difference within the sample reduces the potential drop in the junction between the tip and sample. This phantom force is an apparently repulsive force caused by a decrease in the electrostatic attraction between tip and sample. If the total resistance within the tip or sample is high enough, then the phantom force can be the dominant contrast mechanism in AFM images. It can also dominate features in bias and distance spectroscopy. This chapter includes a comprehensive description of our theory of the phantom force and data which demonstrate this effect.

## 5.1 Introduction and Background

The most exciting aspect of scanning tunneling microscopy (STM) is that images can be acquired with spatial resolution on the atomic scale [1]. STM is not a microscopy technique in the typical sense, with lenses used to optically focus a beam, but rather uses a sharp tip to locally probe surfaces and adsorbates [2]. A voltage difference is applied between the atomically-sharp tip and the surface, and although they are not

A.J. Weymouth (✉) · F.J. Giessibl
University of Regensburg, 31 Universitaetsstrasse, 93053 Regensburg, Germany
e-mail: jay.weymouth@ur.de

F.J. Giessibl
e-mail: Franz.Giessibl@physik.uni-regensburg.de



S. Morita et al. (eds.), *Noncontact Atomic Force Microscopy*,
NanoScience and Technology, DOI 10.1007/978-3-319-15588-3_5

touching (the tip is up to a few atomic diameters away from the surface), electrons tunnel through the vacuum gap. Because tunneling occurs mainly through the apex atom of the tip, the STM can achieve spatial resolution on the atomic scale.

In a tunneling event, an electron (either to or from the tip) tunnels across the vacuum gap into an unoccupied state. It is this process that is most often considered in the STM community, and theoretical techniques based upon this consideration are the groundwork for understanding STM data [3, 4]. However, two other processes also occur: The electron will not remain localized where it first arrived but will rather conduct to the bulk, as will the corresponding hole.

Because of the high local concentration of the tunneling current around the front atom of the tip, the areal current density is very large [5]. Ohm's law directly relates the current density to the electrical field via the resistivity of the conductive material. If the tip or the sample has substantial resistivity, then a significant electric field will be present within it. This electric field can equivalently be described by a voltage difference between the surface and the bulk. While it is difficult for STM alone to be sensitive to this, atomic force microscopy (AFM) is.

AFM is sensitive to the total force interaction between the tip and the sample including those contributions resulting from electrostatic interactions. When a substantial fraction of the applied voltage drops within the sample, a smaller fracton thereof drops between the tip and sample. This decreases the electrostatic attraction which can be observed in AFM. We call this effect the phantom force.

The remainder of this section begins with a short description of atomic force microscopy. The forces that dominate AFM measurements at the atomic scale include the chemical binding force, van der Waals force and electrostatic forces. As the phantom force is caused by changes in the electrostatic force, the electrostatic force is discussed in more detail. A key ingredient to our theory is a potential drop within the sample, from the surface below the tip to the bulk. Finally, these ingredients are combined to present the theoretical picture of the phantom force.

### *5.1.1 Frequency-Modulation Atomic Force Microscopy*

Frequency-modulation atomic force microscopy (FM-AFM) is a non-contact AFM technique that is highly sensitive to short-range forces. One advantage of FM-AFM is that frequency is a value that we are able to measure with high precision. Short-range forces, by definition, decay very quickly as a function of distance. Instead of being directly sensitive to the vertical force component $F_{ts}$ between the tip and the sample, FM-AFM is sensitive to the force gradient $k_{ts} = -\mathrm{d}F_{ts}/\mathrm{d}z$.

Throughout this chapter $z$ and vertical refer to distances along the surface normal. Increasing $z$ refers to a greater distance from the surface. Lateral motion refers to motion along the surface, that is, perpendicular to the surface normal.

The tip is attached to a cantilever that can be characterized by an effective spring constant $k$. The forces acting on the tip are a superposition of the cantilever and the tip-sample interaction:

$$F_{ts} = -kz + -k_{ts}z = -(k + k_{ts})z \tag{5.1}$$

The assumption here is that $k_{ts}$ is constant over the oscillation of the cantilever, referred to as the small-amplitude approximation. The cantilever is oscillated in the $z$-direction at its resonance frequency $f_0$. The influence of $k_{ts}$ is detected via a frequency shift $\Delta f = f - f_0$, where $f$ is the actual oscillation frequency. If we consider the tip to have some mass $m$ and the cantilever to be massless, then the frequency

$$f = \frac{1}{2\pi}\sqrt{\frac{k + k_{ts}}{m}}. \tag{5.2}$$

This is also acceptable to the situation where the cantilever has mass, and in this case $m$ is replaced by an effective mass term plus the mass of the tip. Expanding $f$ around $k_{ts} = 0$ in terms of $k_{ts}$:

$$f = f_0 + \frac{f_0}{2k}k_{ts} + O \tag{5.3}$$

Here $O$ represents the higher-order terms (those with $k_{ts}^2$ terms and above). If the force gradient is constant over the cantilever oscillation, one can write:

$$\Delta f = \frac{f_0}{2k}k_{ts} \tag{5.4}$$

This approximation is the small-amplitude approximation. In order to convert the frequency shift into the force between tip and sample, $k_{ts}$ must be calculated from $\Delta f$, and then integrated from a point far from the surface (that is, where the tip-sample interaction can be assumed to be zero) to the point of interest. In the case of a conservative force field, the force can be integrated to yield the potential energy.

If the force gradient cannot be assumed to be constant over one tip oscillation, then the relation between $\Delta f$ and $k_{ts}$ includes a weighting of $k_{ts}$ over the cantilever oscillation. $\Delta f$ is then written as

$$\Delta f = \frac{f_0}{2k}\langle k_{ts}\rangle, \tag{5.5}$$

where the angled brackets represent a weighted average, described in more detail in [6]. In this case, evaluation of $F_{ts}$ requires a deconvolution of $\Delta f$ followed by an integration step. Two methods for this deconvolution and integration include the Sader-Jarvis deconvolution method [7] and Giessibl's matrix method [8]. For a comparison of the two methods, the reader is directed to [9].

In general, the frequency shift $\Delta f$ can be interpreted as follows: an increase in $\Delta f$ indicates a repulsive contribution to the force, whereas a decrease in $\Delta f$ indicates an attractive contribution.

### 5.1.2 The Forces at Play at the Atomic Scale

Many forces can play a significant role in atomic-scale AFM, but we focus on the chemical interaction of the apex atom with the sample, the van der Waals interaction and electrostatic interactions.

Historically, it is the chemical interaction between tip and sample that was first believed to be responsible for atomic resolution in AFM images [10, 11]. A complete description of chemical bonds is quite complex, including overlapping orbitals and rehybridization. An approximation of the interaction between single atoms is given by the Morse potential, which describes attraction between two atoms up to an equilibrium distance, and then the subsequent repulsion. This overall behavior can also be modelled by a Lennard-Jones potential. Recently high-resolution AFM results have shown that both can very accurately model certain tip-sample interactions [12, 13].

The van der Waals force describes the interaction between two induced dipoles. This interaction is surprisingly well-described by the Hamaker approximation, in which all interacting particles are assumed to interact independently. The van der Waals interaction can dominate at the nanometer-scale. The force-distance relationship of the van der Waals interactions have been explicitly calculated for a number of high-symmetry AFM tips [14].

The description of the long-range electrostatic force comes from considering the tip-sample junction as a capacitor, where the presence of a potential difference causes attractive interaction. This model is appropriate for metallic surfaces. In a macroscopic picture, this results from both the work function differences of the two materials (discussed in the next section) and any applied voltage. Semiconductors are more challenging, in that the electric field cannot be assumed to fully drop over the junction, but rather penetrates significantly into the sample. This effect has been well-studied in the framework of STM and is known as Tip Induced Band-Bending (TIBB) [15]. For all sample systems, even insulators, it is common to apply a voltage to minimize this macroscopic electrostatic force.

These three forces are a good foundation for interpreting most AFM data. The electrostatic and van der Waals forces are expected to increase in magnitude and stay attractive as the tip approaches the surface. The chemical interaction is expected to dominate at short-range with an attractive bond followed by repulsion caused by Pauli repulsion. This picture is what makes the phantom force so confusing: one expects repulsive contrast only at very small tip-sample distances that are closer than the chemical bonding distance. However this phantom force, as presented in more detail in Sect. 5.1.6, can also appear to be a repulsive force that can be mistaken for Pauli repulsion.

### 5.1.3 Electrostatic Attraction Between Metal Surfaces

The electrostatic attraction between two flat metal surfaces depends upon the potential between them. This is a function of the applied voltage, as well as the differences in their work functions. The energy necessary to remove an electron from a solid at 0 K is the work function, $\Phi$. Two materials far from each other will share vacuum levels, however there is no requirement that their Fermi levels align. This occurs when they are put in electrical contact with each other. If they do not have the same work function, then a potential difference will exist between the two metal surfaces.

Different crystal facets have different values of $\Phi$, and we understand these differences in terms of surface dipoles, $p_s$, that cover a surface with an areal density $n_p$. Considering the potential in the vertical dimension,

$$\Phi = E_F + \frac{q_e}{\varepsilon_0} p_s n_p \tag{5.6}$$

where $q_e$ is the elementary charge and $E_F$ is the Fermi level.

Writing the total potential difference within the tip-sample junction as the sum of the differences in work function and of any applied voltage:

$$V_J = V_B + \Delta\Phi \tag{5.7}$$

To consider the effect of this to a FM-AFM setup, we can consider a geometrically simple arrangement, in which both tip and surface are two parallel plates, with area $A$. The magnitude of the electric field between the two is given as

$$|\mathbf{E}| = E = V_J/z \tag{5.8}$$

where the distance between the plates is $z$. The potential energy, $U_{PE}$, stored in the electric field can be calculated by the total work, $W$, required to create the charge distribution. In a conservative field, this yields the following:

$$-U_{PE} = W = \frac{\varepsilon_0}{2}\int_V |E|^2 dV = \frac{\varepsilon_0}{2}\left(\frac{V_J}{z}\right)^2 zA = \frac{\varepsilon_0}{2} V_J^2 \frac{A}{z} \tag{5.9}$$

If we have a purely conservative force, then the interaction force between the two plates would be given by the negative gradient of the energy. The $z-$component of the electrostatic force can be written:

$$F_{es} = -\frac{\mathrm{d}U_{PE}}{\mathrm{d}z} = -\frac{\varepsilon_0}{2} V_J^2 \frac{A}{z^2} \tag{5.10}$$

That is, there will be an attractive force that is proportional to the potential difference squared. Capacitance $C$ is as a measure of the charge on each surface $Q$ as a function of the potential difference, $C = Q/V_J$. For a general case, the attractive force can

be rewritten as a function of capacitance:

$$F_{es} = \frac{1}{2}\frac{\mathrm{d}C}{\mathrm{d}z}V_J^2 \tag{5.11}$$

In the typical picture of long-range electrostatic interactions, this interaction does not vary over the surface. In Kelvin Probe Force Microscopy (KPFM), one measures the electrostatic interactions locally by varying the applied voltage:

$$F_{es} = \frac{1}{2}\frac{\mathrm{d}C}{\mathrm{d}z}(V_B + \Delta\Phi)^2 \tag{5.12}$$

This picture, while widely used, does not include the effect of the phantom force, which is discussed in the next section.

### *5.1.4 Conductance in an Atomic-Scale Junction*

To consider the conductance within the sample, we started with an Ohmic model [16]. Under this model, there is a linear relationship between current density, $\mathbf{j}$, and electric field, characterized by the resistivity $\rho$:

$$\mathbf{E} = \rho\mathbf{j} \tag{5.13}$$

Given that there is a current from the point of the surface where the electrons tunnel either to or from the tip, $\mathbf{r}_0$, and the bulk, $\mathbf{r}_1$, there must be an electric field present (as there must be a force upon the charge carriers) and therefore a potential as well. The potential

$$\phi = -\int_{\mathbf{r}_0}^{\mathbf{r}_1}\mathbf{E}\cdot\mathrm{d}\mathbf{r} = -\int_{\mathbf{r}_0}^{\mathbf{r}_1}\rho\mathbf{j}\cdot\mathrm{d}\mathbf{r} = -\int_{\mathbf{r}_0}^{\mathbf{r}_1}\rho\frac{\mathbf{I}}{A}\cdot\mathrm{d}\mathbf{r} \tag{5.14}$$

If we assume nothing other than a radial current flow, then the vectors can be omitted and

$$\phi = -\int_{r_0}^{r_1}\rho\frac{I}{A}\mathrm{d}r = -\int_{r_0}^{r_1}\rho\frac{I}{2\pi r^2}\mathrm{d}r = -\rho I\left(\frac{1}{2\pi r_1} - \frac{1}{2\pi r_0}\right) \tag{5.15}$$

For the case where $r_1 = \infty$ is the bulk, and $r_0$ is the radius of the tunneling current, $\phi$ can be simplified:

$$\phi = -\frac{\rho I}{2\pi r_0} \tag{5.16}$$

We will consider a piece of silicon, doped to have a resistivity of $\rho_{Si} = 10\,\Omega\,\mathrm{cm}$. We assume that the tunneling current is a cylindrical stream with a radius of $r_0 = 100$

pm. The effective sample resistance is then

$$R_S = \frac{\phi}{I} = \frac{1\,\Omega\,\mathrm{cm}}{2\pi \cdot 100\,\mathrm{pm}} = 159\,\mathrm{M}\Omega. \tag{5.17}$$

The Ohmic model is usually accepted as a model for bulk transport, so one would naturally ask how relevant it is to atomic-scale transport. Recent work from the Simmons group indicates that for Si wires doped with P, this law does hold down to the atomic scale [17].

One failure of the Ohmic model is that it does not represent the electronic band structure. In the case of Si(111)−7×7, for example, the surface has a metallic surface state within the band gap of the bulk Si crystal [18]. Transport from the surface to the bulk has been extensively studied [19, 20] and is neither Ohmic nor constant over the surface [21]. While this is correct, the Ohmic model nevertheless explains the majority of our observations, and we expect inclusion of the electronic structure to simply increase the accuracy of the phantom force model.

This model provides an understanding of the systems where we expect non-negligable phantom force effects to be observed. A tunneling current of $I = 1\,\mathrm{nA}$ through low-doped Si will result in a voltage difference of 0.159 V between the tip-sample junction and the bulk. This is a significant fraction of the voltage that is normally applied while scanning this surface. On the other hand, metallic surfaces like Cu have a resistivity of $\rho_{Cu} \approx 2 \times 10^{-8}\,\Omega\,\mathrm{m}$. This would result in a sample resistance of $R_S = 0.32\,\Omega$, and a negligible voltage drop within the sample.

### 5.1.5 *Including Resistance in Our Overall Picture of Tunneling*

The sample resistance describes the effect of the sample on the current within it. The total current, therefore, will no longer be a function just of the applied bias voltage and the effective resistive drop in the tunneling junction,[1] but rather include the resistive sample component described by the phantom force:

$$I = \frac{V_B}{R_J + R_S} \tag{5.18}$$

This sample resistance will also act as a voltage divider. That is, the potential difference between tip and sample does not simply include contributions from the applied bias voltage $V_B$ and the difference in work functions:

$$V_J = V_B + \Delta\Phi - I R_S = V_B \frac{R_J}{R_J + R_S} + \Delta\Phi \tag{5.19}$$

[1] Tunneling is an elastic process but the effect of tunneling and then a quick energetic relaxation is often modelled by a resistor.

The effect of sample resistance on an AFM image is via the electrostatic force:

$$F_{es} = \frac{1}{2}\frac{\mathrm{d}C}{\mathrm{d}z}V_J^2 \tag{5.20}$$

And so, in terms of the junction resistance:

$$F_{es} = \frac{1}{2}\frac{\mathrm{d}C}{\mathrm{d}z}\left(V_B\frac{R_J}{R_J + R_S} + \Delta\Phi\right)^2 \tag{5.21}$$

And as a function of the current:

$$F_{es} = \frac{1}{2}\frac{\mathrm{d}C}{\mathrm{d}z}(V_B + \Delta\Phi - IR_S)^2 \tag{5.22}$$

In order to determine the regime in which the phantom force is significant, we rewrite the tunneling current junction resistance depending exponentially upon the tip-sample distance:

$$R_J = R_0 \exp[2\kappa z] \tag{5.23}$$

$\kappa$ is the decay constant of the tunneling current, which is usually around $1\,\text{Å}^{-1}$ [2]. If $z = 0\,\text{m}$ denotes the position where the tip and sample are in chemical contact, then $R_0$ is the resistance at point contact. This has been very well measured for the case of metal-metal single-atom contacts in break-junction measurements [22] and is known to be $1/G_0$, where $G_0$ is the quantum-point conductance. The phantom force starts to play a noticeable role when the sample (or tip) resistivity $R_S$ becomes comparable to the junction resistance $R_J$. For example, if the junction resistance is $1\,\text{G}\Omega$ (1 V and 1 nA), then a sample resistance of $R_S = 159\,\text{M}\Omega$ cannot be ignored. From (5.23), we expect this to happen at tip-sample distances of $z < 0.6\,\text{nm}$, which is a typical distance for AFM images.

### *5.1.6 Summary*

The phantom force is an effect that can be observed when a tunneling current is present in force measurements, and there is a substantial resistance for the current from the point of tunneling to the bulk. It can be represented by an internal sample resistance, as sketched in Fig. 5.1. For low-doped Si samples, this resistance can be on the order of $100\,\text{M}\Omega$.

An internal resistance can also be present in the tip. Morita et al. reported measurements of the tunneling current while using $\Delta f$ to regulate tip height [23]. Before poking a clean W tip into a Si surface, they recorded a current of 16 nA at 0.2 V. After a tip poke, with the same feedback parameters, the current was less than the noise floor of 5 pA at a voltage of 0.1 V. This indicates an additional resistance of $20\,\text{G}\Omega$.

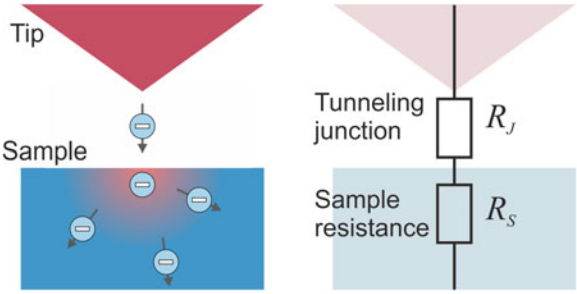


**Fig. 5.1** A net tunneling current flows because there is a potential difference between the tip and sample. In this drawing, the tip has a higher potential for electrons and they tunnel to the sample. Electrons then disperse from the point of entry to the bulk. A similar process occurs in the tip (not shown). The overall effect depends strongly on the material's ability to conduct electrons from this point to the bulk. This can be modelled by the addition of a sample resistance $R_S$

In order to demonstrate the effect of the phantom force, we can explicitly model three contributions to the overall force: the van der Waals force, the electrostatic force, and the chemical interaction. The van der Waals contribution is modelled as suggested by Giessibl [14] with a conic tip that has an opening angle of $\alpha = 70°$, using a Hamaker coefficient of $A_H = 0.1865\,\text{aJ}$. The chemical interaction was modelled with a Morse potential having a bonding energy of $E_B = 4\,\text{eV}$, an equilibrium distance of $z_0 = 200\,\text{pm}$, and a decay constant of $\lambda = 100\,\text{pm}$[2]:

$$E_{\text{Morse}} = E_B \left( \exp -\frac{2(z - z_0)}{\lambda} - 2\exp -\frac{(z - z_0)}{\lambda} \right) \tag{5.24}$$

The electrostatic force is modelled as suggested by Guggisberg et al. [25], with an opening angle of $\alpha = 70°$, a final tip radius of $r_{tip} = 4\,\text{nm}$, a tip length of 1 mm, and an offset distance between the final apex atom and the part of the tip that contributes significantly to the electrostatic force of $z_{off} = 1\,\text{nm}$. A sketch of this tip model is shown in Fig. 5.4. The voltage is the junction voltage, as described by (5.19), with a bias of $V_B = 1\,\text{V}$ and a contact potential difference of $\Delta\Phi = -0.2\,\text{V}$.

Each of these contributions is individually shown in Fig. 5.2a. The van der Waals contribution is attractive over the entire range. The chemical bond contribution only becomes significant with distances $z < 1\,\text{nm}$. The electrostatic contribution, although at further distances is simply attractive, also changes suddenly at $z < 1\,\text{nm}$. At this point, $R_J \approx R_S$.

The effect of the phantom force is also evident in the total force interaction, shown in Fig. 5.2b, and in the force gradient, shown in Fig. 5.2c. Although the total force gradient decreases with decreasing tip-sample distance, the phantom force causes a first minimum followed by a zero-crossing. This first minimum can therefore be

[2]These parameters were chosen as representative. Bond lengths from 100 to 300 pm are common, as are dissociation energies on the order of a few eV [24].

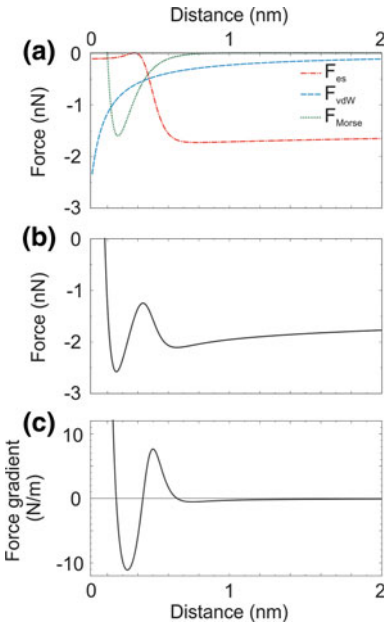


**Fig. 5.2** Out of the three forces discussed in Sect. 5.1.2, the electrostatic force changes the strongest when the phantom force is present. **a** A model of the $z$ dependance of the electrostatic force, van der Waals force, and chemical interaction (represented by a Morse potential). **b** The total force *curve*. Note the two local minima, in contrast to what is normally expected. **b** A corresponding plot of the force gradient, calculated from the *curve* in **b**. Again there is a second local minimum

incorrectly attributed to the equilibrium distance of the chemical interaction, although it is several hundred picometers further.

It is therefore easy to mistake an effect of the phantom force as an observation of chemical interaction, especially as tunneling is usually localized over atomic sites.

## 5.2 Observations

Silicon was the first material upon which we observed the phantom force. We were imaging at room temperature and noticed when we collected constant-height data that the adatoms appeared repulsive. This on its own was surprising, as the reactive nature of the surface also makes it ideal to investigate adsorbates [26, 27].[3] While we expected differences in the adatom types [29, 30], the contrast we observed very closely resembled the contrast in our STM images.

Since these initial observations, we have recorded observations at both liquid He-temperature (with an Omicron low-temperature SPM system, operating nominally at 4.5 K) and at room temperature (with a homebuilt microscope, modelled after the Park Scientific Instruments UHV system [31]). We used two types of Si samples: a highly doped sample with a resistivity of 0.010–0.012 Ω cm at 300 K, and a lower doped sample with a resistivity of 6–9 Ω cm at 300 K.

[3]It should be noted that Sweetman et al. have reported repulsive contrast over the Si(111)−7×7 surface, which can occur with non-reactive tip apexes [28].

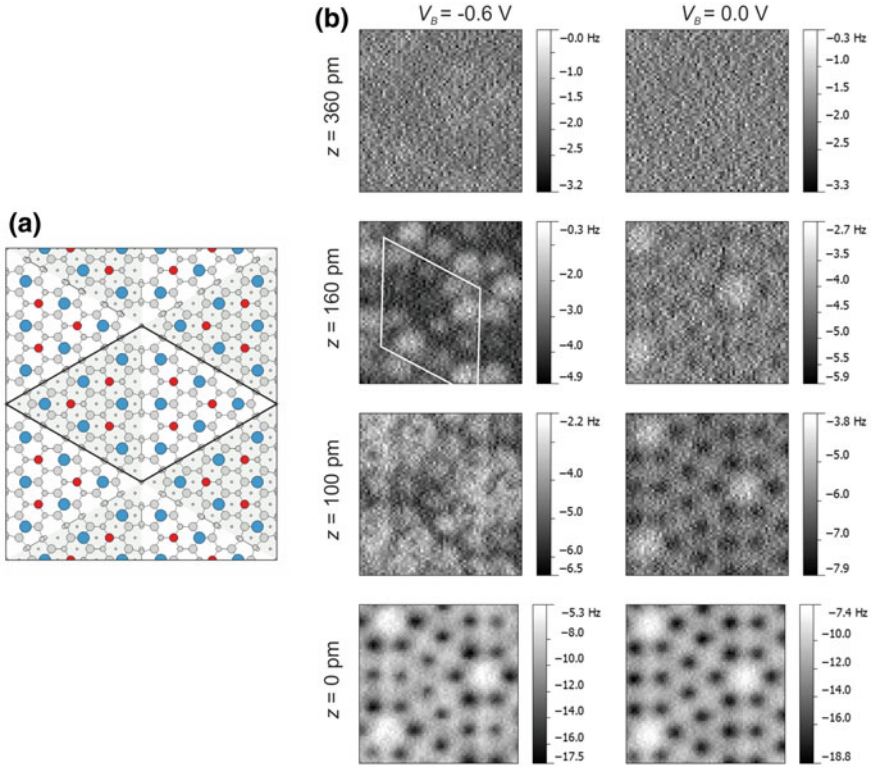


**Fig. 5.3** **a** Schematic of the Si(111)−7×7 surface. Nominally, only the Si adatoms (*blue*) are observable by AFM and STM. **b** Constant-height FM-AFM data taken with and without an applied bias voltage at various heights $z$. $z = 0$ pm is the point of closest approach

Figure 5.3 shows two series' of AFM images at various tip-sample distances, one with an applied voltage of −0.6 V and the second with an applied voltage of 0.0 V. At $z = 160$ pm, contrast can be seen in both datasets. In the dataset with $V_B = -0.6$ V, the adatoms appear repulsive. In the dataset with $V_B = -0.0$, the area over the adatoms appears more attractive than the area over the corner holes. The repulsive contrast is attributed to the phantom force, whereas the attractive contrast is attributed to the chemical interaction. This trend continues with closer approach, as the chemical interaction stars to dominate. At $z = 0$ m, the images appear similar.

A second experiment (also at liquid-He temperature) demonstrates the effect of the phantom force, shown in Fig. 5.4. At standard STM conditions of a voltage of 1.5 V and a current of 2 nA, contrast can be observed in the AFM channel in constant-height mode. This is again due to the phantom force. When the voltage is decreased to 0 V, the contrast disappears. In order to observe the expected attractive contrast, we need to approach the tip 340 pm closer to the surface.

Several questions naturally arise with this data. We have presented a theory based upon the internal sample resistance, however there are other phenomena at play

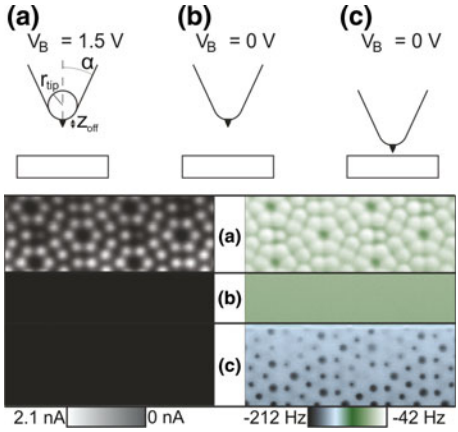


**Fig. 5.4** Constant-height FM-AFM data. The *top third* was acquired with a voltage $V = 1.5\,\mathrm{V}$ at a relative tip height of $z = 340\,\mathrm{pm}$. The *middle third* was acquired with no applied voltage at $z = 340\,\mathrm{pm}$. The *lower third* was acquired with no applied voltage at $z = 0\,\mathrm{m}$. Adapted from [16]

that could cause contrast inversion or, at the least, a strong bias dependance: 1. We could be changing the tip-sample distance by changing the bias and probing repulsive interaction due to a chemical bond. 2. This effect could be related to tip-induced band bending. 3. This could all be an artifact from a poorly-chosen STM preamplifier. None of these three are acceptable explanations, for the following reasons.

1. In Fig. 5.4, the tip must be approached to the surface 340 pm before attractive chemical interaction can be observed. If the contrast in the upper third of the image was caused by repulsive chemical interaction, then removal of the bias voltage must result in the average cantilever height being increased by over 340 pm. We used a qPlus sensor with a spring constant of $k = 1800\,\mathrm{N/m}$, meaning that a force difference of 612 nN is required. With the calculations presented in Sect. 5.1.6, the electrostatic forces are one hundred times too low for this to be feasible.

2. Tip-induced band bending is a description of the field effect of the tip when probing a semiconducting surface [32, 33]. However, in the case of Si(111)−7×7, it is weakly present [34]. The surface reconstruction presents a metallic surface state, and therefore the field effect of the tip is greatly reduced. Of course, this means that we must now demonstrate that the phantom force is not unique to this special case, which we present later for the case of H-terminated Si(100).

3. If the STM preamplifier was poorly selected, then the virtual ground would be insufficient. In that case, a current could result in a significant deviation from 0 V, and also reduce the attractive electrostatic force. The simplest test for this was to install a switch where we could change from using the virtual ground to using a real ground. The result is presented in [35], but to summarize, we observed no difference in the two. This does not mean that the virtual ground cannot affect AFM measurements, it simply means that the deviation of the virtual ground provided by the STM preamplifier from an ideal ground is not responsible for the phantom force.

In the rest of this section, the data collected on Si(111)−7×7 is used to quantitatively extract values of $R_S$. The effect of the phantom force on Kelvin probe force microscopy is demonstrated and discussed. Data is shown of the phantom force on the

H-terminated Si(100) surface. Finally, we show data that indicate that the phantom force is present even on molecular adsorbates that lie on highly conductive surfaces.

### 5.2.1 Characterizing the Phantom Force

While the previous two examples demonstrate qualitatively the effect of the phantom force, they do not provide a quantitative measurement of the phantom force. One method to do this is by investigating the relationship between the recorded current $\langle I \rangle$ and $\Delta f$. We published these results in [16]; here we review them. The recorded current is written $\langle I \rangle$ because it is the average current over the oscillation of the cantilever. All data taken in this subsection were acquired at room temperature.

In Fig. 5.5, constant-height data of low-doped Si(111)−7×7 are shown at both bias polarities: In (a) and (b), $V_B = +1.5\,\mathrm{V}$ and in (c) and (d), $V_B = -1.5\,\mathrm{V}$. The AFM images show an increase in $\Delta f$ above the adatoms in the unit cell, irrespective of the polarity of the bias voltage. The data show strong similarity to the STM data, with adatoms of the faulted half of the unit cell appearing brighter when probing filled-state images. While this is expected in STM data [21], it is surprising that the contrast in the AFM image would also be so dependent upon $V_B$.

As we simultaneously measure $\langle I \rangle$ and $\Delta f$, we can directly compare the two, pixel-by-pixel. One technical detail is that the relative bandwidths of the two measurements must be taken into account. Even with a relatively high bandwidth of the phase-locked loop (AFM controller) of $B = 120\,\mathrm{Hz}$, it is much lower than the

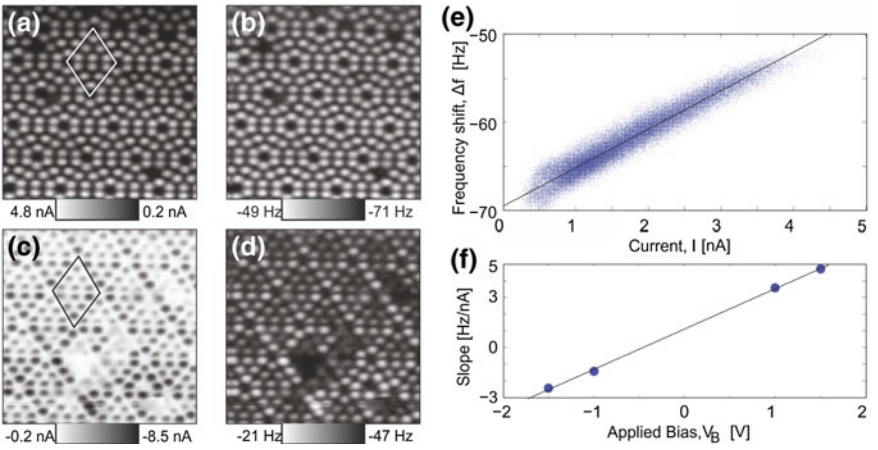


**Fig. 5.5** Constant-height data taken at room temperature with simultaneous $\langle I \rangle$ and $\Delta f$. **a** and **b** taken at $V_B = +1.5\,\mathrm{V}$, **c** and **d** taken at $V_B = -1.5\,\mathrm{V}$. **e** Pixel-by-pixel plot of $\Delta f$ as a function of $\langle I \rangle$ from data in **a** and **b** with a linear fit. **f** Slopes of the linear fits as a function of the bias voltage follow themselves a linear relation. Adapted from [16]

STM measurements, which can be assumed to be instantaneous in comparison.[4] This will result in a pixel shift between the STM and AFM images. At a scan speed of $v = 20\,\text{nm/s}$, the offset is $\Delta x = v/B = 166\,\text{pm}$.

The corresponding points are shown in Fig. 5.5e. The trend is linear and a fit line is shown. We can understand this linear relation in terms of the Phantom force, within a small amplitude approximation. As we consider only the contrast mechanism, we consider only the contribution to $k_{ts}$ from the electrostatic force[5]:

$$k_{ts} = -\frac{\mathrm{d}F_{es}}{\mathrm{d}z} = -\frac{\mathrm{d}}{\mathrm{d}z}\frac{1}{2}\frac{\mathrm{d}C}{\mathrm{d}z}(V_B + \Delta\Phi - I R_S)^2 \tag{5.25}$$

$$k_{ts} = -\frac{1}{2}\frac{\mathrm{d}^2C}{\mathrm{d}z^2}(V_B + \Delta\Phi - IR_S)^2 + \frac{\mathrm{d}C}{\mathrm{d}z}(V_B + \Delta\Phi - I R_S)\left(R_S\frac{\mathrm{d}I}{\mathrm{d}z}\right) \tag{5.26}$$

In order to write $k_{ts}$ as a polynomial in terms of $I$, we must rewrite the last term as a polynomial in terms of $I$. Substituting (5.18) into $\frac{\mathrm{d}I}{\mathrm{d}z}$:

$$\frac{\mathrm{d}I}{\mathrm{d}z} = \frac{\mathrm{d}}{\mathrm{d}z}\frac{V_B}{R_J + R_S} = \frac{\mathrm{d}}{\mathrm{d}z}\frac{V_B}{R_0\exp[2\kappa z] + R_S} \tag{5.27}$$

$$\frac{\mathrm{d}I}{\mathrm{d}z} = -\frac{V_B}{R_0\exp[2\kappa z] + R_S}\frac{R_0\exp[2\kappa z]}{R_0\exp[2\kappa z] + R_S} \tag{5.28}$$

$$\frac{\mathrm{d}I}{\mathrm{d}z} = -2\kappa I\frac{R_J}{R_J + R_S} \tag{5.29}$$

Rewriting $k_{ts}$ as a polynomial of current:

$$\begin{aligned} k_{ts} = &-\frac{1}{2}\frac{\mathrm{d}^2C}{\mathrm{d}z^2}(V_B + \Delta\Phi)^2 + \\ &+\left[\frac{\mathrm{d}^2C}{\mathrm{d}z^2} - 2\kappa\frac{R_J}{R_J + R_S}\frac{\mathrm{d}C}{\mathrm{d}z}\right](V_B + \Delta\Phi)\,R_S\,I + \\ &+\left[-\frac{1}{2}\frac{\mathrm{d}^2C}{\mathrm{d}z^2} + 2\kappa\frac{R_J}{R_J + R_S}\frac{\mathrm{d}C}{\mathrm{d}z}\right]R_S^2\,I^2 \end{aligned} \tag{5.30}$$

[4] Our STM signal is recorded at 500 Hz.

[5] A complete description of the forces would require consideration of the van der Waals and chemical interactions as well. But, as shown in Fig. 5.4, these do not contribute to the contrast in the AFM image. Therefore it suffices to consider only the electrostatic interaction.

If we assume that the tip is relatively far from the surface and $R_J \gg R_S$:

$$\frac{R_J}{R_J + R_S} \approx 1 \tag{5.31}$$

$k_{ts}$ can then be simplified:

$$\begin{aligned} k_{ts} = &- \frac{1}{2}\frac{\mathrm{d}^2 C}{\mathrm{d}z^2}(V_B + \Delta\Phi)^2 + \\ &+ \left[\frac{\mathrm{d}^2 C}{\mathrm{d}z^2} - 2\kappa\frac{\mathrm{d}C}{\mathrm{d}z}\right](V_B + \Delta\Phi)\, R_S\, I + \\ &+ \left[-\frac{1}{2}\frac{\mathrm{d}^2 C}{\mathrm{d}z^2} + 2\kappa\frac{\mathrm{d}C}{\mathrm{d}z}\right] R_S^2\, I^2 \end{aligned} \tag{5.32}$$

Finally, arguing that $R_S I < 1$, which is valid for $R_S \approx 100\,\mathrm{M\Omega}$ and $I = 1\,\mathrm{nA}$, then $R_S I \gg R_S^2 I^2$:

$$\begin{aligned} k_{ts} &\approx -\frac{1}{2}\frac{\mathrm{d}^2 C}{\mathrm{d}z^2}(V_B + \Delta\Phi)^2 + \left[\frac{\mathrm{d}^2 C}{\mathrm{d}z^2} - 2\kappa\frac{\mathrm{d}C}{\mathrm{d}z}\right](V_B + \Delta\Phi)\, R_S\, I \\ k_{ts} &\approx b + m\, R_S\, I \end{aligned} \tag{5.33}$$

where $b$ and $m$ represent terms independant of $R_S$ and $I$. The slope $m R_S$ is plotted in Fig. 5.5f. In agreement with (5.33), this term varies linearly with $V_B$.

In order to extract a value for $R_S$, we added additional external resistances, $R_{ext}$, to the circuit. While the phantom force is a physical effect caused by the local conductance, addition of an external resistor will cause the same effect, and from (5.33), $k_{ts}$ now can be rewritten:

$$k_{ts} \approx b + m\,(R_S + R_{ext})\, I \tag{5.34}$$

We collected simultaneous $\langle I \rangle$ and $\Delta f$ data for three values of external resistors: $R_{ext} = 0\,\Omega$, $10\,\mathrm{M\Omega}$ and $30\,\mathrm{M\Omega}$, shown in Fig. 5.6.

A linear fit at $R_{ext} = 0\,\Omega$ and $10\,\mathrm{M\Omega}$ yielded a predicted value of $m(R_S + 30\,\mathrm{M\Omega}) = -0.99\,\mathrm{Hz/nA}$.

The observed slope was $-1.03\,\mathrm{Hz/nA}$. This outstanding agreement is a statement to the accuracy of this simple model. In it, we have neglected the weighted average $\langle k_{ts} \rangle$ and used simply a small amplitude approximation $\Delta f \propto k_{ts}$. For the amplitudes used in imaging, $A = 400\,\mathrm{pm}$, this is rarely accurate when probing chemical interactions. However, the electrostatic force has a much weaker distance dependance. We have also approximated $\langle I \rangle \approx I$. This is slighty inaccurate, as $\langle I \rangle$ is 14 % of the peak tunneling current [6].

From the fit, we can extract a value for $R_S$ of $164\,\mathrm{M\Omega}$. This also agrees very well with our predicted value of $159\,\mathrm{M\Omega}$, derived in (5.17).

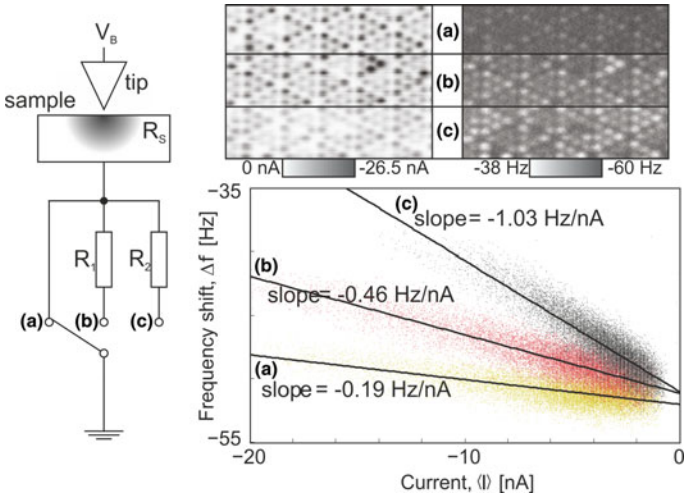


**Fig. 5.6** Adding additional external resistors, $R_1$ and $R_2$, allows us to characterize $R_S$. Simultaneous $\langle I \rangle$ and $\Delta f$ data collected at $V_B = -1.5\,\mathrm{V}$ with **a** $R_{ext} = 0\,\Omega$ **b** $R_{ext} = R_1 = 10\,\mathrm{M\Omega}$, and **c** $R_{ext} = R_2 = 30\,\mathrm{M\Omega}$. Adapted from [16]

It is important that the contrast in these images was due only to the electrostatic interaction. This was verified by the observation that under normal STM imaging conditions, only the phantom force produces contrast in constant-height images, as discussed in the previous subsection. That the images were taken at constant height also confirms that the contrast is not due to the long-range van der Waals component.

### *5.2.2 Kelvin Probe Force Microscopy*

Kelvin Probe Force Microscopy (KPFM) is based on the idea that the difference in the work functions of two metals, $\Delta\Phi$, can be determined by measuring the force between the two as a function of an applied bias voltage, as described in (5.12).

Practically, it is performed in one of two ways. In the conceptually simplest approach, $\Delta f$ is recorded at a fixed tip position as a function of $V_B$. The apex of the resulting parabola is a measure of the local work function, $\Delta\Phi_L$. An alternate method, inspired by the so-called vibrating capacitor method, was introduced by Nonnenmacher and coworkers [36], in which the system is excited with an AC voltage at a frequency $f_0$ and the response is measured at $2f_0$. We will focus on the first method because it contains all relevant physics and is the technique that we performed in this set of experiments.

Similar to AFM imaging, KPFM data can be very susceptible to phantom force effects. Starting from (5.21), the extremum of the parabola will not be $\Delta\Phi_L$, but rather dependant upon $R_S$:

$$-V_B = \Delta\Phi_L \frac{R_J + R_S}{R_J} \tag{5.35}$$

The danger, of course, is that this is not simply a sample property $\Delta\Phi_L$ but also contains a distance dependant term, $R_J$. As the tip approaches the sample, $R_J$ decreases and $\Delta\Phi_L$ appears to increase in magnitude.

There is a further complication because we are sensitive not to forces but to force gradients. Equation (5.26) describes the electrostatic component of the force gradient, and consists of two terms. The first term includes $\frac{\mathrm{d}^2C}{\mathrm{d}z^2}$, which is positive,[6] and a quadratic term which is positive. Therefore

$$-\frac{1}{2}\frac{\mathrm{d}^2C}{\mathrm{d}z^2}(V_B + \Delta\Phi - IR_S)^2 \leq 0 \tag{5.36}$$

Normally this is the only term that is considered in KPFM. However, there is a second term of opposite sign. Because both $\frac{\mathrm{d}C}{\mathrm{d}z}$ and $\frac{\mathrm{d}I}{\mathrm{d}z}$ (as discussed in (5.29)) are negative,

$$\frac{\mathrm{d}C}{\mathrm{d}z}(V_B + \Delta\Phi - IR_S)\left(R_S\frac{\mathrm{d}I}{\mathrm{d}z}\right) \geq 0 \tag{5.37}$$

When performing KPFM with low resistance samples, this term can be ignored, as $R_S \approx 0\,\Omega$.

We performed bias-spectroscopy at low temperature on the Si(111)−7×7 surface. Figure 5.7 shows the simultaneously-collected $\langle I\rangle$ and $\Delta f$ images, as well as $\langle k_{ts}\rangle$ spectra for various tip-sample distances. The $z$ distances are relative to the imaging height. Curves were offset to show the shape easier. The strong $z$-dependance of the curvature of the parabolae is due to the $\frac{\mathrm{d}I}{\mathrm{d}z}$ term, which increases with decreasing tip-sample height, dominating the $\langle k_{ts}\rangle$ data with positive curvature.

We applied a model of the tip as a sphere as described by Hudlet et al. [37]. Similar to the model described in Sect. 5.1.6, we added a $z-$offset term that accounts for the fact that the electrostatic interaction is dominated by a component several atomic layers higher than the imaging apex. The results of the model are shown as dashed lines in Fig. 5.7c, with a tip radius of 4.0 nm, a $z-$offset value of 0.7 nm, and a tunnel current decay constant of $\kappa = 0.9 \times 10^{10}\,\mathrm{m}^{-1}$.

This model very accurately describes the significant feature in the data, that is, the upward-turning of the parabolae at smaller tip-sample distances. The accuracy, especially at larger tip-sample distances, could probably be increased with a more complex geometric model of the tip. At $z = 200$ pm, the shape of the curve seems to deviate from a parabola. This could be due to the electronic structure discussed earlier; in other words, a limitation of the simple Ohmic model.

[6] If this is not clear, consider a parallel plate capacitor with $C = \varepsilon A z^{-1}$. The first derivative with $z$ is negative, and the second is positive.

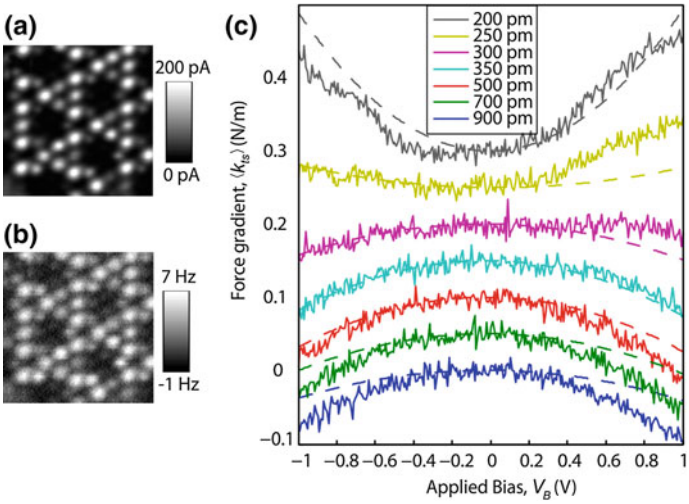


**Fig. 5.7** Constant-height **a** $\langle I \rangle$ and **b** $\Delta f$ images. **c** Kelvin parabolae taken over an adatom at various $z$ distances. Reprinted with permission from A.J. Weymouth and F.J. Giessibl, Appl. Phys. Lett. 101, 213105 (2012), Copyright 2012, AIP Publishing LLC

### *5.2.3 Observations on H-Terminated Si(100)*

The unsaturated Si(100) surface, when prepared in vacuum, reconstructs into rows of Si dimers [39]. This surface is quite reactive, making it experimentally difficult to work with, especially at room temperature. Exposing Si(100) to hydrogen saturates the unsaturated dangling bonds [40]. The electronic states of the hydrogenated dimers have been shown to lie outside the bandgap of bulk Si [41], meaning that in contrast to Si(111)−7×7, the surface is semiconducting. Under normal preparation, not all Si atoms are saturated but a few unsaturated reactive dangling bonds are left.

We compare data taken in which it is the dominant imaging mechanism, shown schematically in Fig. 5.8a, to AFM data collected at low bias, shown in Fig. 5.8d. Figure 5.8b and c show simultaneous AFM and STM data collected with a bias of 1.5 V. In them, the dimer rows can be seen running from upper left to lower right. The low contrast is due to the fact that we did not want to encounter a tunneling current that was too high when scanning over the defect area, circled in red. This is a dangling bond, which we would expect to observe in AFM data as attractive. However due to the increase of the tunneling current over it, the phantom force effect causes an increase in $\Delta f$ that makes it appear repulsive. This attractive interaction is clearly observed in AFM data collected at low bias, as shown in Fig. 5.8e. (The red circle has been laterally offset to account for drift.) Not only is the atomic structure of the surface visible, as shown by the spacefill model overlaid in the lower third of the image, but the defect now appears as attractive.

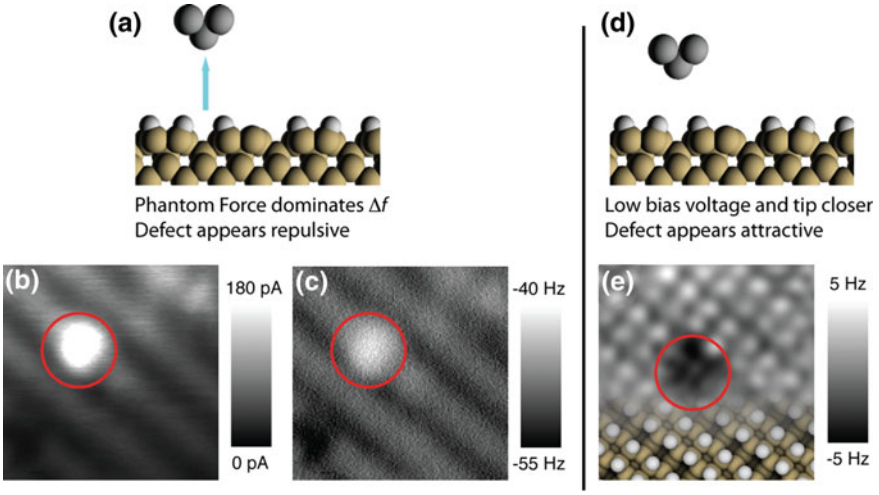


**Fig. 5.8** When the tip is far from the surface with an applied bias of 1.5 V, (**a**) atomic contrast can be observed in STM, (**b**) and AFM data, (**c**). The defect outlined in *red* appears repulsive. However, at close tip-sample distances, (**d**) and low bias, in this case 200 mV, it appears attractive, (**e**). (Plane subtraction and low-pass filtering have been applied to **e** for clarity.) Images are 3 nm × 3 nm [38]

### *5.2.4 Molecular Adsorbate on Graphene*

The $R_S$ term in our theory describes the sample resistance that is internal and therefore decreases the voltage in the junction. This resistance can be due to resistivity of a bulk sample, and it can also be due to a smaller resistive element on the surface.

Graphene has one of the highest electron mobilities of any material. We have investigated graphene grown on SiC, supplied by Th. Seyller's workgroup [42], with low temperature AFM and STM. On some samples, we come across adsorbates that we can manipulate with the tip. We propose that these adsorbates are hydrocarbon molecules that are either a biproduct of the manufacturing or a natural contaminant that is introduced when we fix the graphene samples to appropriate holders.

Figure 5.9 shows constant-height $\Delta f$ data of one of these adsorbates, both (a) with and (b) without an applied bias voltage. This dataset was collected by moving the tip over each line first with an applied bias and then without. Most of the image shows very similar contrast, however, there is a lobe on the lower left that appears brighter in Fig. 5.9a. We compared a line scan over this lobe from the two images, as shown in Fig. 5.9c.

The area with greater $\Delta f$ corresponds to a region where the current was greater. Because these adsorbates are easy to manipulate with the tip, they are likely not strongly coupled to the surface. This weak coupling could be the physical explanation of the potential drop from the point on the molecule into which electrons tunnel, and the rest of the surface, where the electrons can rapidly move into equilibrium.

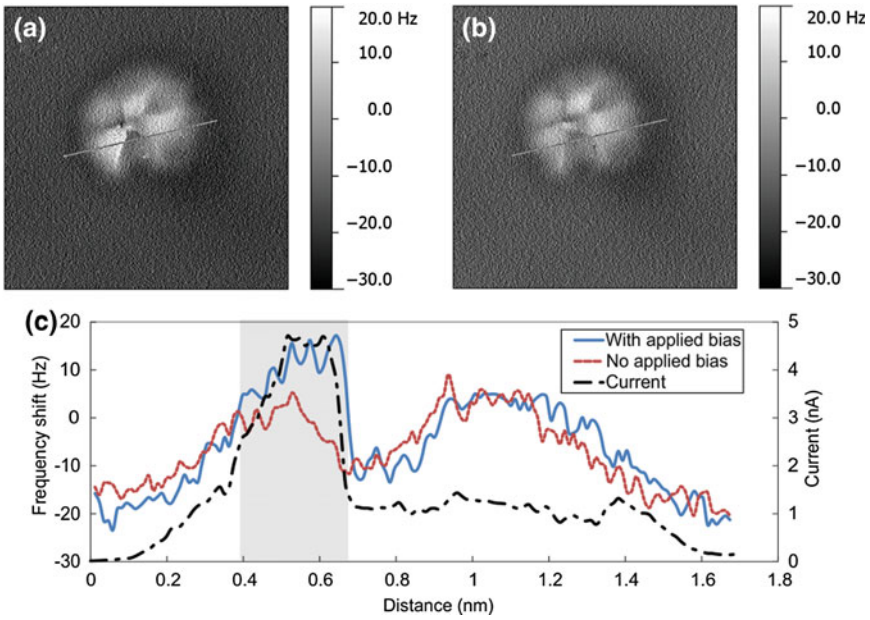


**Fig. 5.9** Constant height measurements reveal a difference in $\langle k \rangle_{ts}$ images as a function of bias voltage. **a** With an applied bias of 0.4 V. **b** 0 V. **c** A linescan comparing the two $\langle k \rangle_{ts}$ data and the corresponding current

## 5.3 Concluding Remarks and Outlook

There are several mentions in literature of AFM contrast inversion as a function of the applied bias voltage, and therefore, of the current. The three reviewed here are investigations of the Si(111)−7×7 surface. Molitor et al. reported contrast inversion depending upon scan parameters [43]. While scanning in STM mode (with an undriven thermal amplitude of $A = 30\,\text{pm}$ and an applied bias of 1.1 V) they report a decrease of $\Delta f$ over the adatoms. When scanning in AFM mode, using $\Delta f$ to regulate the tip height (and a driven amplitude of $A = 20\,\text{nm}$, and a voltage of 1.9 V), they observe contrast inversion in the $\Delta f$ image. Arai and Tomitori compared data taken with and without an applied voltage [44]. They note that differences between the adatom species can be seen with the applied voltage, but not without. At higher applied voltages, the authors observe contrast inversion of the AFM signal. Guggisberg et al. also reported inverted AFM contrast as a function of the applied voltage [45]. They note that at a sample bias of 2 V, the AFM signal is inverted and moreover, that the features correlate very well with the recorded tunneling current data. They compare this image to one taken at −1 V, where the contrast is not inverted.

One explanation for all these observations is the phantom force. In Sect. 5.2.1, we present data in which the $\Delta f$ images appear similar to STM data as a function of bias voltage. This similar contrast is because when probing the filled states

of Si(111)−7×7, the tunnelling current is higher over the faulted half. Therefore, differences in the adatoms can be observed that is equivalent to that seen in STM images.

It is important to note that the occurrence of the phantom force does not require that the tunneling current is measured. Rather, it is due to an additional resistance outside the tip-sample junction. By adding external resistors, as discussed in Sect. 5.2.1, we were able to quantify this additional resistive element.

We present a model based upon a Ohmic mechanism of conductance that explains our observed images and spectra. It's likely that this can also explain previous reports of contrast inversion in AFM as a function of voltage. While most of our observations have demonstrated the phantom force on surfaces of semiconductors, we also presented data where it appears to be present on a molecular adsorbate. As AFM studies continue, and are coupled with a drive to understand the electronic structure of surface and adsorbates, the phantom force is an effect which must be taken into account.

**Acknowledgments** A.J.W. thanks J. Repp and T. Arai for helpful discussions, as well as B. Drevniok for his helpful comments of the manuscript. The authors acknowledge T. Wutscher for his great contributions to the phantom force work.

## References

1. G. Binnig, H. Rohrer, C. Gerber, E. Weibel, Phys. Rev. Lett. **50**(2), 120 (1983)
2. G. Binnig, H. Rohrer, Rev. Mod. Phys. **71**(2), S324 (1999)
3. J. Tersoff, D. Hamann, Phys. Rev. B **31**, 805 (1985)
4. J.M. Blanco, F. Flores, R. Pérez, Prog. Surf. Sci. **81**(10–12), 403 (2006)
5. G. Binnig, H. Rohrer, C. Gerber, E. Weibel, Phys. Rev. Lett. **49**(1), 57 (1982)
6. F.J. Giessibl, Rev. Mod. Phys. **75**(3), 949 (2003)
7. J.E. Sader, S.P. Jarvis, Appl. Phys. Lett. **84**(10), 1801 (2004)
8. F.J. Giessibl, Appl. Phys. Lett. **78**, 123 (2001)
9. J. Welker, E. Illek, F.J. Giessibl, Beilstein J. Nanotechnol. **3**, 238 (2012)
10. F.J. Giessibl, Science **267**(5194), 68 (1995)
11. R. Pérez, I. Štich, M. Payne, K. Terakura, Phys. Rev. B **58**(16), 10835 (1998)
12. N. Moll, L. Gross, F. Mohn, A. Curioni, G. Meyer, New J. Phys. **12**(12), 125020 (2010)
13. A.J. Weymouth, T. Hofmann, F.J. Giessibl, Science **343**, 1120 (2014)
14. F.J. Giessibl, Phys. Rev. B **56**(24), 16010 (1997)
15. R.M. Feenstra, Y. Dong, M.P. Semtsiv, W.T. Masselink, Nanotechnology **18**(4), 044015 (2007)
16. A.J. Weymouth, T. Wutscher, J. Welker, T. Hofmann, F.J. Giessibl, Phys. Rev. Lett. **106**(22), 226801 (2011)
17. B. Weber, S. Mahapatra, H. Ryu, S. Lee, A. Fuhrer, T.C.G. Reusch, D.L. Thompson, W.C.T. Lee, G. Klimeck, L.C.L. Hollenberg, M.Y. Simmons, Science **335**(6064), 64 (2012)
18. R. Losio, K.N. Altmann, F.J. Himpsel, Phys. Rev. B **61**, 10845 (2000)
19. J. Mysliveček, A. Stróecka, J. Steffl, P. Sobotík, I. Oštádal, B. Voigtländer, Phys. Rev. B **73**, 161302(R) (2006)
20. P. Jelínek, M. Švec, P. Pou, R. Perez, V. Cháb, Phys. Rev. Lett. **101**(17), 176101 (2008)
21. R.J. Hamers, R.M. Tromp, J.E. Demuth, Phys. Rev. Lett. **56**(18), 1972 (1986)
22. N. Agrait, J. Rodrigo, S. Vieira, Phys. Rev. B **47**(18), 12345 (1993)
23. K.I. Morita, Y. Sugimoto, M. Abe, S. Morita, Appl. Phys. Express **4**(11), 115201 (2011)

24. D.R. Lide (ed.), *CRC Handbook of Chemistry and Physics, Internet Version 2005* (CRC Press, Boca Raton, 2005)
25. M. Guggisberg, M. Bammerlin, C. Loppacher, O. Pfeiffer, A. Abdurixit, V. Barwich, R. Bennewitz, A. Baratoff, E. Meyer, H.J. Güntherodt, Phys. Rev. B **61**(16), 11151 (2000)
26. R.A. Wolkow, P. Avouris, Phys. Rev. Lett. **60**(11), 1049 (1988)
27. A.J. Weymouth, R.H. Miwa, G.J.A. Edge, G.P. Srivastava, A.B. McLean, Chemical Communications (Cambridge, England) **47**(28), 8031 (2011)
28. A. Sweetman, P. Rahe, P. Moriarty, Nano Lett. **14**(5), 2265 (2014)
29. M.A. Lantz, H.J. Hug, R. Hoffmann, P.J. van Schendel, P. Kappenberger, S. Martin, A. Baratoff, H.J. Güntherodt, Science **291**(5513), 2580 (2001)
30. J. Welker, A.J. Weymouth, F.J. Giessibl, ACS Nano **7**(8), 7377 (2013)
31. F.J. Giessibl, B.M. Trafas, Rev. Sci. Instrum. **65**(6), 1923 (1994)
32. R. Feenstra, G. Meyer, K. Rieder, Phys. Rev. B **69**(8), 081309(R) (2004)
33. V. Ramachandran, R.M. Feenstra, Phys. Rev. Lett. **82**, 1000 (1999)
34. M. McEllistrem, G. Haase, D. Chen, R.J. Hamers, Phys. Rev. Lett. **70**(16), 2471 (1993)
35. T. Wutscher, A.J. Weymouth, F.J. Giessibl, Phys. Rev. B **85**(19), 195426 (2012)
36. M. Nonnenmacher, M.P. OBoyle, H.K. Wickramasinghe. Appl. Phys. Lett. **58**(25), 2921 (1991)
37. S. Hudlet, M. Saint Jean, C. Guthmann, J. Berger, Eur. Phys. J. B **2**(1), 5 (1998)
38. T. Wutscher, Untersuchung der Kopplung von atomaren Strömen und atomaren Kräften durch die Rastersondenmikroskopie. Ph.D. thesis, Universität Regensburg (2012)
39. D.J. Chadi, Phys. Rev. Lett. **43**(1), 43 (1979)
40. J.J. Boland, Phys. Rev. Lett. **65**(26), 3325 (1990)
41. H. Raza, Phys. Rev. B **76**(4), 045308 (2007)
42. K.V. Emtsev, A. Bostwick, K. Horn, J. Jobst, G.L. Kellogg, L. Ley, J.L. McChesney, T. Ohta, S.A. Reshanov, J. Röhrl, E. Rotenberg, A.K. Schmid, D. Waldmann, H.B. Weber, T. Seyller, Nat. Mater. **8**(3), 203 (2009)
43. S. Molitor, P. Güthner, T. Berghaus, App. Surf. Sci. **140**(3–4), 276 (1999)
44. T. Arai, M. Tomitori, Appl. Surf. Sci. **157**(4), 207 (2000)
45. M. Guggisberg, O. Pfeiffer, S. Schär, V. Barwich, M. Bammerlin, C. Loppacher, R. Bennewitz, A. Baratoff, E. Meyer, App. Phys. A Mater. Sci. Proc. **72**(S1), S19 (2001)